Opto-Electronic Science

CN 51-1800/O4 ISSN 2097-0382 (Print) ISSN 2097-4000 (Online)

Direct detection with an optimal transfer function: toward the electrical spectral efficiency of coherent homodyne detection

Xingfeng Li, Jingchi Li, Xiong Ni, Hudi Liu, Qunbi Zhuge, Haoshuo Chen, William Shieh and Yikai Su

Citation: Li XF, Li JC, Ni X, et al. Direct detection with an optimal transfer function: toward the electrical spectral efficiency of coherent homodyne detection. *Opto-Electron Sci* **4**, 240020 (2025).

https://doi.org/10.29026/oes.2025.240020

Received: 21 July 2024; Accepted: 12 October 2024; Published online: 24 December 2024

Related articles

High-speed multiwavelength InGaAs/InP quantum well nanowire array micro-LEDs for next generation optical communications

Fanlu Zhang, Zhicheng Su, Zhe Li, Yi Zhu, Nikita Gagrani, Ziyuan Li, Mark Lockrey, Li Li, Igor Aharonovich, Yuerui Lu, Hark Hoe Tan, Chennupati Jagadish, Lan Fu

Opto-Electronic Science 2023 **2**, 230003 doi: 10.29026/oes.2023.230003

31.38 Gb/s GaN-based LED array visible light communication system enhanced with V-pit and sidewall quantum well structure

Zengyi Xu, Wenqing Niu, Yu Liu, Xianhao Lin, Jifan Cai, Jianyang Shi, Xiaolan Wang, Guangxu Wang, Jianli Zhang, Fengyi Jiang, Zhixue He, Shaohua Yu, Chao Shen, Junwen Zhang, Nan Chi

Opto-Electronic Science 2023 **2**, 230005 doi: 10.29026/oes.2023.230005

Efficient stochastic parallel gradient descent training for on-chip optical processor

Yuanjian Wan, Xudong Liu, Guangze Wu, Min Yang, Guofeng Yan, Yu Zhang, Jian Wang

Opto-Electronic Advances 2024 **7**, 230182 doi: 10.29026/oea.2024.230182

More related article in Opto-Electronic Journals Group website

Opto-Electronic Science

http://www.oejournal.org/oes

OE_Journal

Website

Opto-Electronic Science

Article

February 2025, Vol. 4, No. 2

DOI: 10.29026/oes.2025.240020 CSTR: 32246.14.oes.2025.240020

Direct detection with an optimal transfer function: toward the electrical spectral efficiency of coherent homodyne detection

Xingfeng Li[1], Jingchi Li[1], Xiong Ni[1], Hudi Liu[1], Qunbi Zhuge[1], Haoshuo Chen[2], William Shieh[3] and Yikai Su[1]*

Complex-valued double-sideband direct detection (DD) can reconstruct the optical field and achieve a high electrical spectral efficiency (ESE) comparable to that of a coherent homodyne receiver, and DD does not require a costly local oscillator laser. However, a fundamental question remains if there is an optimal DD receiver structure with the simplest design to approach the performance of the coherent homodyne detection. This study derives the optimal DD receiver structure with an optimal transfer function to recover a quadrature amplitude modulation (QAM) signal with a near-zero guard band at the central frequency of the signal. We derive the theoretical ESE limit for various detection schemes by invoking Shannon's formula. Our proposed scheme is closest to coherent homodyne detection in terms of the theoretical ESE limit. By leveraging a WaveShaper to construct the optimal transfer function, we conduct a proof-of-concept experiment to transmit a net 228.85-Gb/s 64-QAM signal over an 80-km single-mode fiber with a net ESE of 8.76 b/s/Hz. To the best of our knowledge, this study reports the highest net ESE per polarization per wavelength for DD transmission beyond 40-km single-mode fiber. For a comprehensive metric, denoted as 2^{ESE}×Reach, we achieve the highest 2^{ESE}×Reach per polarization per wavelength for DD transmission.

Keywords: optical communication; direct detection; optical field recovery; electrical spectral efficiency

Li XF, Li JC, Ni X et al. Direct detection with an optimal transfer function: toward the electrical spectral efficiency of coherent homodyne detection. *Opto-Electron Sci* **4**, 240020 (2025).

Introduction

Driven by bandwidth-hungry Internet services, such as artificial intelligence (AI) video streaming, e-commerce, and social networks, traffic demands for data center interconnections and metro networks have experienced exponential growth[1–3]. Coherent detection is a promising candidate owing to its superior performance, including its capability for field reconstruction and high electrical spectral efficiency (ESE)[4–6]. However, an expensive narrow-linewidth local oscillator (LO) laser is required at the receiver, which inevitably increases the system cost. Consequently, intensity modulation-direct detection (IM-DD) is still widely implemented as a low-cost solution for short-reach applications[7]. However, the conventional IM-DD system sacrifices approximately half of the ESE because only the amplitude is used as the modulation dimension. Additionally, various impairments, such as the chromatic dispersion (CD), cannot be digitally

[1]State Key Lab of Advanced Optical Communication Systems and Networks, Department of Electronic Engineering, Shanghai Jiao Tong University, Shanghai 200240, China; [2]Nokia Bell Labs, 600 Mountain Ave, Murray Hill, NJ 07974, USA; [3]School of Engineering, Westlake University, Hangzhou 310030, China.

*Correspondence: YK Su, E-mail: yikaisu@sjtu.edu.cn

Received: 21 July 2024; Accepted: 12 October 2024; Published online: 24 December 2024

compensated owing to the lack of field recovery capability, which significantly limits the attainable bitrate-reach product[8]. Although single-sideband (SSB) modulation based on the Kramers–Kronig (KK) algorithm can be used to extend the transmission distance, the ESE is limited because the carrier is located at the edge of the signal spectrum and the image sideband bears no information[9,10]. Additionally, a Stokes-vector receiver (SVR) with field reconstruction was proposed, but its ESE is still far from that of coherent homodyne detection[11,12]. A carrier-less phase retrieval receiver was proposed to recover the phase of a quadrature amplitude modulation (QAM) signal based on a modified Gerchberg-Saxton (GS) algorithm[13]. However, the carrier-less phase retrieval receiver must fully detect the signal-to-signal beat interference (SSBI), which doubles the required receiver electrical bandwidth, compared with that of a coherent homodyne receiver, thus limiting the ESE. Consequently, it is worthwhile to investigate the field recovery of complex-valued double-sideband (CV-DSB) signals using DD. More specifically, the advanced detection scheme should have the following characteristics: (i) capability of field recovery for digital impairment compensation, (ii) high ESE, that is, a capability to detect CV-DSB signals, and (iii) a low-cost solution that does not require an LO laser.

Recently, carrier-assisted differential detection (CADD) was proposed to recover the full field of a CV-DSB signal based on a delay interferometer structure[14]. Both the left sideband (LSB) and right sideband (RSB) of the CV-DSB signal were loaded with uncorrelated information-bearing signals. On the receiver side, the CADD receiver recovers the CV-DSB signal from the carrier-signal beating term instead of the SSBI term. Subsequently, similar technologies were proposed, such as integrated silicon photonic (SiP) CADD receivers[15–17], asymmetric self-coherent detection (ASCD) receivers[18,19], Jones space direct detection (JSDD) receivers[20,21], and as discussed in our previous studies, deep-learning-enabled DD (DLEDD) receivers[22–25]. However, a common problem in all the aforementioned approaches for CV-DSB DD is the periodic frequency nulls induced by the imperfect transfer functions of the receivers, which originates from the CD element or delay interferometer. The frequency nulls induce severe SSBI enhancement, which distorts the desired linear carrier-signal beating term and demands wide frequency guard bands, thereby sacrificing the achievable system data rate and ESE. In ref.[26], a DD receiver with a near-ideal phase response was demonstrated by using a racetrack resonator. The highest ESE of 7.1 b/s/Hz was achieved using the integrated DD receiver. However, a fundamental question remains if there is an optimal DD receiver structure with the simplest design to approach the performance of the coherent homodyne detection. In coherent homodyne detection, the quadrature component is detected based on the beating between the 90-degree phase-shifted carrier and the information-bearing signal.

In this paper, via analogy to coherent homodyne detection, we derived an optimal DD receiver architecture comprising a coupler, two single-ended photodiodes (PDs), two analog-to-digital converters (ADCs), and a frequency-selective phase shifter with an optimal transfer function, explaining why the structure in ref.[26] is ideal. Our proposed scheme advances the field in the following aspects: (i) starting from the receiver structure of coherent homodyne detection, the optimal DD receiver structure is derived to approach the performance of coherent homodyne detection through the simplest design, (ii) compared to a fixed phase shift, an adjustable phase shift on either the carrier or the information-bearing signal enables better performance by considering the impact of SSBI, and (iii) we use a convolutional neural network (CNN) to seamlessly achieve signal reconstruction and SSBI mitigation in a unified step. By invoking Shannon's formula, we derive the theoretical ESE limits for the various detection schemes. The proposed scheme is closest to the coherent homodyne scheme. The simulation results indicate that our proposed scheme has only an approximately 1-dB optical signal-to-noise ratio (OSNR) penalty at the 25% forward error correction (FEC) threshold compared with that of a coherent transmission system, considering the carrier-to-signal power ratio (CSPR) penalty. Additionally, we perform a proof-of-concept experiment in which a WaveShaper (WS) is employed to construct the optimal transfer function. By judiciously selecting the appropriate phase shift, we successfully demonstrate a 46-GBaud 64-QAM signal in an 80-km single-mode fiber (SMF) transmission experiment with 228.85-Gb/s net data rate and 8.76-b/s/Hz net ESE. In the context of data center interconnections, metro networks, and mobile backhauls beyond 40 km[27–29], we report the highest net ESE per polarization per wavelength on DD transmission, to the best of our knowledge. For a comprehensive metric, denoted as 2^{ESE}×Reach, we also achieved the highest 2^{ESE}×Reach per polarization per wavelength on DD transmission.

Results

Evolution from coherent homodyne detection to direct detection

We start the analysis from a conventional phase-diversity coherent homodyne receiver. Figure 1(a) shows the configuration, which consists of a laser, a 90° optical hybrid, and two balanced photodiodes (BPDs). The received information-bearing signal is $s(t)$. When the signal and LO are co-polarized, four outputs can be obtained after the 90° optical hybrid, as follows:

$$E_1 = \frac{1}{2}(s + c) \ , \tag{1}$$

$$E_2 = \frac{1}{2}(s - c) \ , \tag{2}$$

$$E_3 = \frac{1}{2}(s + \mathrm{j}c) \ , \tag{3}$$

$$E_4 = \frac{1}{2}(s - \mathrm{j}c) \ , \tag{4}$$

where j denotes an imaginary unit. Without loss of generality, we assume that the carrier c is a real-valued constant.

Then, the output photocurrents from the PDs are given by

$$i_1 = |E_1|^2 = \frac{1}{4}\left\{|s|^2 + |c|^2 + 2\,\mathrm{Re}\left(s \cdot c^*\right)\right\} \ , \tag{5}$$

$$i_2 = |E_2|^2 = \frac{1}{4}\left\{|s|^2 + |c|^2 - 2\,\mathrm{Re}\left(s \cdot c^*\right)\right\} \ , \tag{6}$$

$$i_3 = |E_3|^2 = \frac{1}{4}\left\{|s|^2 + |c|^2 + 2\,\mathrm{Im}\left(s \cdot c^*\right)\right\} \ , \tag{7}$$

$$i_4 = |E_4|^2 = \frac{1}{4}\left\{|s|^2 + |c|^2 - 2\,\mathrm{Im}\left(s \cdot c^*\right)\right\} \ , \tag{8}$$

where * represents conjugation. Re[·] and Im[·] denote the real and imaginary parts, respectively. After the two BPDs, the in-phase and quadrature components of $s(t)$ can be reconstructed as follows:

$$s_{\text{in-plases}} = i_1 - i_2 = \mathrm{Re}\left(s \cdot c^*\right) \ , \tag{9}$$

$$s_{\text{quadrature}} = i_3 - i_4 = \mathrm{Im}\left(s \cdot c^*\right) \ . \tag{10}$$

Different from coherent detection, carrier-assisted DD with a copropagating carrier is an LO-free detection scheme, as depicted in Fig. 1(b). We assume that the received optical signal is $[s(t) + c]/2$, where c and $s(t)$ represent the carrier and information-bearing signals, respectively. Next, we impose a phase shift on the carrier. More specifically, the carriers are imposed by 180°, 90°, and −90° phase shifts at the second, third, and fourth reception paths, respectively. The phase responses of the $h_1(t)$, $h_2(t)$, and $h_3(t)$ are shown in Fig. 1(c). After imposing phase shifts on the carrier, we can obtain the same fields as expressed in Eqs. (1–4). We can then recover the information-bearing signal, similar to a coherent detection. Two BPDs are used to eliminate the SSBI and $|c|^2$. Consequently, Fig. 1(b) illustrates an optimal DD receiver that achieves the same performance as that of a coherent homodyne.

However, the optimal DD receiver depicted in Fig. 1(b) is complicated because three frequency-selective phase shifters are required. If SSBI is mitigated in digital signal processing (DSP) algorithms, the optimal DD receiver structure can be simplified, as shown in Fig. 2(a).

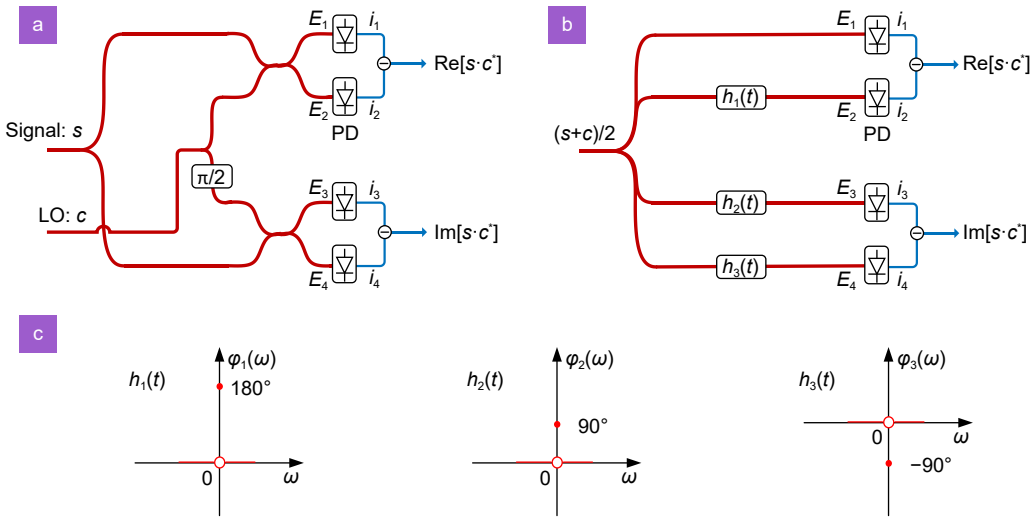

Fig. 1 | (**a**) Configuration of the phase-diversity coherent homodyne receiver. (**b**) Optimal DD receiver with three frequency-selective phase shifters. (**c**) Phase responses of $h_1(t)$, $h_2(t)$, and $h_3(t)$.

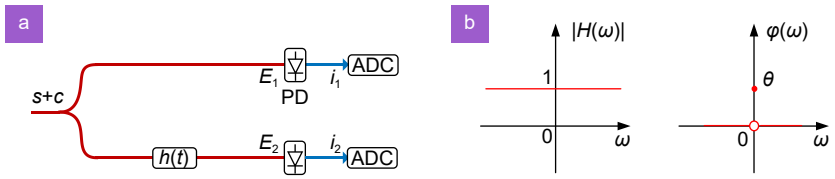

Fig. 2 | Proposed DD receiver with the optimal transfer function. (**a**) Optimal receiver structure. (**b**) Optimal amplitude and phase responses of $h(t)$.

It consists of a coupler, a frequency-selective phase shifter, two single-ended PDs, and two ADCs, explaining why the structure in ref.[26] is ideal. Without loss of generality, we use θ to present the phase shift. Figure 2(b) shows the amplitude and phase responses of $h(t)$. For the sake of simplicity, we assume that the received optical signal is $s(t) + c$. We hereafter also consider the impact of noise on the performance. The fields before the PDs are as follows:

$$E_1 = s + c\,, \tag{11}$$

$$E_2 = s + \mathrm{e}^{\mathrm{j}\theta}c\,. \tag{12}$$

After the square-law detection, the output photocurrents can be written as

$$\begin{aligned} i_1 =& |E_1|^2 + n_1 = |s|^2 + |c|^2 + 2\mathrm{Re}(s\cdot c^*) + n_1 \\ =& |s|^2 + |c|^2 + 2cs_{\text{in-phase}} + n_1\,, \end{aligned} \tag{13}$$

$$\begin{aligned} i_2 =& |E_2|^2 + n_2 = |s|^2 + |c|^2 \\ &+ 2\mathrm{Re}(s\cdot \mathrm{e}^{-\mathrm{j}\theta}\cdot c^*) + n_2 \\ =& |s|^2 + |c|^2 + 2\mathrm{Re}[(s_{\text{in-phase}} + \mathrm{j}s_{\text{quadrature}}) \\ &\cdot(\cos\theta - \mathrm{j}\sin\theta)\cdot c^*] + n_2 \\ =& |s|^2 + |c|^2 + 2c(s_{\text{in-phase}}\cos\theta + s_{\text{quadrature}}\sin\theta) \\ &+ n_2\,, \end{aligned} \tag{14}$$

where n_1 and n_2 denote the uncorrelated white Gaussian noises. We can reconstruct the in-phase and quadrature components of the information-bearing signal as follows:

$$s_{\text{in-phase}} = \frac{i_1 - |s|^2 - |c|^2 - n_1}{2c}\,, \tag{15}$$

$$s_{\text{quadrature}} = \frac{i_2 - |s|^2 - |c|^2 - 2c\cdot s_{\text{in-phase}}\cdot\cos\theta - n_2}{2c\cdot\sin\theta}\,. \tag{16}$$

The carrier c can reach the optimum value via a direct-current-sweep method. This method is widely used in KK and CADD receivers. In addition, the direct-current component can also be recovered by using an alternating current-coupled PD[30].

The structure is simplified at the cost of introducing the SSBI, as shown in Eqs. (15) and (16). If the SSBI can be eliminated via DSP, the recovery error of the quadrature component in Eq. (16) is $\dfrac{2c\cdot s_{\text{in-phase}}\cdot\cos\theta + n_2}{2c\cdot\sin\theta}$. To minimize the recovery error and thus maximize the electrical SNR (ESNR) of the recovered signal, the optimum phase shift is 90°, which is in good agreement with the coherent receiver in Eqs. (9) and (10). In practice, an iterative algorithm is used to mitigate the SSBI. We can use a recursive feedback algorithm to mitigate the SSBI, as shown in Fig. 3. In the first iteration, based on Eqs. (15) and (16), the SSBI and linear crosstalk $2cs_{\text{in-phase}}$ are set to zero. The recovered field $s(t)$ is used to estimate the $|s(t)|^2$ and $2cs_{\text{in-phase}}$, which are removed from i_1 and i_2 according to Eqs. (15) and (16) during the second iteration. This process is carried out iteratively until the impacts of SSBI and linear crosstalk are marginal.

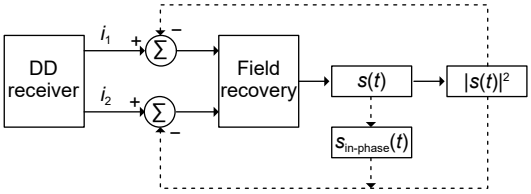

Fig. 3 | Schematic diagram of the iterative SSBI cancellation algorithm.

After each iteration, the resulting signals are as follows:

Iteration 1:

$$s_{\text{in-phase1}} = \frac{i_1 - |c|^2}{2c}\,,$$

$$s_{\text{quadrature1}} = \frac{i_2 - |c|^2}{2c\cdot\sin\theta}\,,$$

$$s_1 = s_{\text{in-phase1}} + \mathrm{j}s_{\text{quadrature 1}}\,.$$

The recovery error is $e_1 = (s_{\text{in-phase1}} - s_{\text{in-phase}}) + \mathrm{j}(s_{\text{quadrature1}} - s_{\text{quadrature}}) = \dfrac{|s|^2 + n_1}{2c} + \mathrm{j}\dfrac{|s|^2 + 2c\cdot s_{\text{in-phase}}\cdot\cos\theta + n_2}{2c\cdot\sin\theta}$.

The loss function is

$$\begin{aligned} |e_1|^2 =& \left|\frac{|s|^2 + n_1}{2c} + \mathrm{j}\frac{|s|^2 + 2c\cdot s_{\text{in-phase}}\cdot\cos\theta + n_2}{2c\cdot\sin\theta}\right|^2 \\ =& \left|\frac{|s|^2 + n_1}{2c}\right|^2 + \left|\frac{|s|^2 + 2c\cdot s_{\text{in-phase}}\cdot\cos\theta + n_2}{2c\cdot\sin\theta}\right|^2 \end{aligned}\,.$$

Iteration 2:

$$s_{\text{in-phase2}} = \frac{i_1 - |s_1|^2 - |c|^2}{2c}\,,$$

$$s_{\text{quadrature2}} = \frac{i_2 - |s_1|^2 - |c|^2 - 2c - s_{\text{in-phase1}} \cdot \cos\theta}{2c \cdot \sin\theta},$$

$$s_2 = s_{\text{in-phase2}} + \text{j}s_{\text{quadrature2}}.$$

The recovery error is $e_2 = (s_{\text{in-phase2}} - s_{\text{in-phase}}) + \text{j}(s_{\text{quadrature2}} - s_{\text{quadrature}}) = \frac{|s|^2 - |s_1|^2 + n_1}{2c} + \text{j}\frac{|s|^2 - |s_1|^2 + 2c \cdot (s_{\text{in-phase}} - s_{\text{in-phase1}}) \cdot \cos\theta + n_2}{2c \cdot \sin\theta}$.

The loss function is $|e_2|^2 = \left|\frac{|s|^2 - |s_1|^2 + n_1}{2c}\right|^2 + \left|\frac{|s|^2 - |s_1|^2 + 2c \cdot (s_{\text{in-phase}} - s_{\text{in-phase1}}) \cdot \cos\theta + n_2}{2c \cdot \sin\theta}\right|^2$.

Iteration 3: ……

In Iteration 1, the SSBI is not mitigated. When θ is 90°, the recovery error and the loss function are minimized. In Iteration 2, the SSBI is partially mitigated by using s_1. Since the terms in the quadrature component of e_2 are not the same signs, the optimum θ is related to both the SSBI and noise. As the iteration goes on, the loss function becomes more and more complicated. We will verify that the optimum θ is affected by CSPR and OSNR later.

Phase shift imposed on signal

In addition to imposing a phase shift on the carrier, we confirm that the same result could be obtained by imposing the phase shift on the signal, which yields an alternative transfer function for $h(t)$. The receiver structure remains as illustrated in Fig. 2(a), but the amplitude and phase responses of $h(t)$ are shown in Fig. 4. At the receiver, the incident signal is split into two parts by a 1×2 coupler. The fields before the PDs are as follows:

$$E_1 = s + c, \tag{17}$$

$$E_2 = (s+c) \otimes h(t) = s \otimes h(t) + c \otimes h(t) = \text{e}^{\text{j}\theta}s + c, \tag{18}$$

where $\otimes$ represents the linear convolution. After square-law detection, the output photocurrents can be expressed as

$$\begin{aligned} i_1 &= |E_1|^2 + n_1 = |s|^2 + |c|^2 + 2\,\text{Re}\,(s \cdot c^*) + n_1 \\ &= |s|^2 + |c|^2 + 2cs_{\text{in-phase}} + n_1, \end{aligned} \tag{19}$$

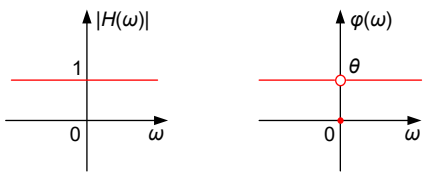

Fig. 4 | Alternative amplitude and phase responses of $h(t)$.

$$\begin{aligned} i_2 &= |E_2|^2 + n_2 = \left|s \cdot \text{e}^{\text{j}\theta}\right|^2 + |c|^2 \\ &\quad + 2\,\text{Re}\left(s \cdot \text{e}^{\text{j}\theta} \cdot c^*\right) + n_2 \\ &= |s|^2 + |c|^2 + 2\text{Re}[(s_{\text{in-phase}} + \text{j}s_{\text{quadrature}}) \\ &\quad \cdot (\cos\theta + \text{j}\sin\theta) \cdot c^*] + n_2 \\ &= |s|^2 + |c|^2 + 2c(s_{\text{in-phase}}\cos\theta - s_{\text{quadrature}}\sin\theta) + n_2. \end{aligned} \tag{20}$$

We can recover the in-phase and quadrature components of the information-bearing signal as follows:

$$s_{\text{in-phase}} = \frac{i_1 - |s|^2 - |c|^2 - n_1}{2c}, \tag{21}$$

$$s_{\text{quadrature}} = -\frac{i_2 - |s|^2 - |c|^2 - 2c \cdot s_{\text{in-phane}} \cdot \cos\theta - n_2}{2c \cdot \sin\theta}. \tag{22}$$

Eqs. (21) and (22) agree with Eqs. (15) and (16). The negative sign is present because the phase difference between the signal and carrier is θ instead of $-\theta$ as in the previous section. In Eq. (22), the recovery error of the quadrature component is $\frac{|s|^2 + 2c \cdot s_{\text{in-phase}} \cdot \cos\theta + n_2}{2c \cdot \sin\theta}$, and it is minimized when θ is 90°. We refer to this process of signal reconstruction as Solution 1. Next, we present Solution 2 to reconstruct the signal.

In Solution 2, the in-phase component is still recovered by using Eq. (21). To recover the quadrature component from Eq. (20), we use Eq. (19) to eliminate the linear crosstalk. We have:

$$\begin{aligned} i_1\cos\theta - i_2 = (|s|^2 + |c|^2 + n_1) \cdot \cos\theta - |s|^2 - |c|^2 + \\ 2cs_{\text{quadrature}} \cdot \sin\theta - n_2\ . \end{aligned} \tag{23}$$

Then, the recovered quadrature component is expressed as:

$$\begin{aligned} s_{\text{quadrature}} = &\frac{1}{2c \cdot \sin\theta}[i_1\cos\theta - i_2 - (|s|^2 + |c|^2 + n_1) \\ &\cdot \cos\theta + |s|^2 + |c|^2 + n_2]. \end{aligned} \tag{24}$$

The recovery error in Eq. (24) is $\frac{1}{2c \cdot \sin\theta}[(|s|^2 + n_1) \cdot \cos\theta - (|s|^2 + n_2)]$. Since the two terms in the square bracket are opposite signs, the optimum θ is related to both the SSBI and noise. There is no definite θ that minimizes the recovery error.

Next, we validate the aforementioned theoretical analysis through a numerical simulation. In the simulation, we generate a 50-GBaud dual-SSB 16-QAM Nyquist-shaped signal with a roll-off factor of 0.01. A 6-GHz guard band (−3 GHz to 3 GHz) is inserted between the LSB and RSB. After loading the additive white Gaussian noise, we use the proposed DD receiver with an optimal transfer function to detect the 16-QAM signal. More

details regarding the simulation setup are provided in Section 1 of Supplementary information. As illustrated in Fig. 5(a), the optimum θ is 90° and the θ is not affected by the CSPR and OSNR. After the iterative SSBI cancellation, the optimum θ experiences minor perturbation, as depicted in Fig. 5(b). For Solution 2, the optimum θ is related to both CSPR and OSNR, regardless of whether the iterative SSBI cancellation algorithm is carried out, as shown in Fig. 5(c) and 5(d). In addition, we observe that the bit error ratio (BER) performance of Solution 2 is better than that of Solution 1, which can be attributed to the fact that the SSBI and linear crosstalk have the same signs in Eq. (22); however, the two SSBI terms have opposite signs in Eq. (24). The ESNR of the recovered signal is improved in Solution 2.

It is anticipated that there might exist alternative solutions capable of achieving superior BER performance compared with that presented in Solution 2. Nevertheless, determining the optimal signal reconstruction method through conventional formula derivations remains a challenge. Our ultimate goal is to obtain the most favorable BER performance after signal reconstruction and SSBI cancellation. Leveraging a CNN is a promising approach for achieving this goal[31]. This approach, illustrated in Fig. 6, is denoted as Solution 3. The two detected photocurrents are fed into the CNN as inputs. We utilize the same deep CNN structure employed in our previous work[25], which is also provided in Section 1 of Supplementary information. This approach enables us to seamlessly achieve signal reconstruction and SSBI mitigation in a unified step through the implementation of the CNN, thus enabling optimal system performance. In this work, ~10^4 real-valued multiplications are required to reconstruct the field of one symbol. If an advanced field-programmable gate array (FPGA) is used, lower 10^8 real-valued multiplications per symbol are feasible for realistic signal processing[32]. To simplify the CNN structure and reduce the algorithm complexity, a pruned algorithm can be utilized[33].

Figure 7(a) shows the BER performance by varying θ at different CSPRs and OSNRs for Solution 3. Note that the BERs are zero for θ varying from 20° to 45° under the conditions of a 6-dB CSPR and 33-dB OSNR, which are not depicted in the figure. The BER performance of Solution 3 is much better than that of Solution 2. The ultimate BER performance is determined by both the residual SSBI and noise (related to the OSNR), where the residual SSBI is dependent on the initial SSBI (related to the CSPR), SSBI enhancement (related to the transfer function of $h(t)$), and SSBI cancellation algorithm. The

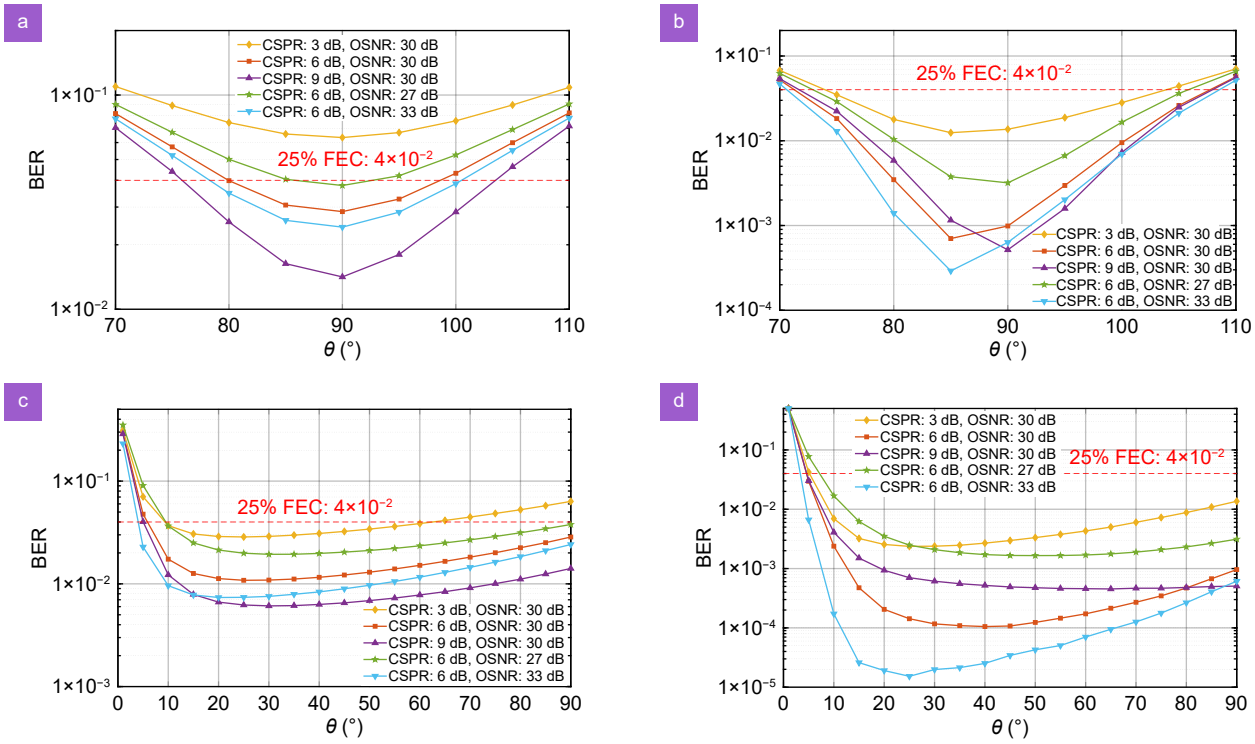

Fig. 5 | Simulated BER versus θ for Solution 1 (**a**) without, and (**b**) with iterative SSBI cancellation. Simulated BER versus θ for Solution 2 (**c**) without, and (**d**) with iterative SSBI cancellation.

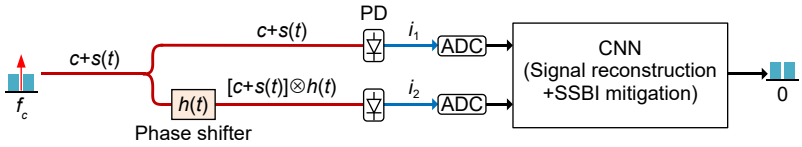

Fig. 6 | Solution 3: signal reconstruction and SSBI mitigation in one step with the CNN.

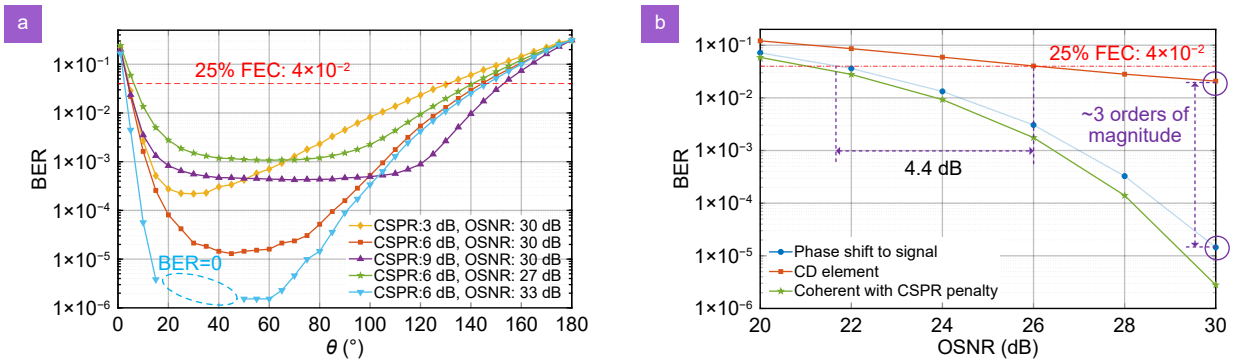

Fig. 7 | Solution 3: (**a**) Simulated BER versus θ at different CSPR and OSNR values. (**b**) Simulated BER versus OSNR for different schemes with a CSPR of 6 dB.

optimum θ is reduced as the SSBI increases or the noise decreases. In short, the optimal receiver structure is shown in Fig. 2(a) to approach the performance of coherent homodyne detection through the simplest design. The corresponding optimal transfer functions $h(t)$ are illustrated in Figs. 2(b) and Fig. 4. In practice, the phase shift needs to be optimized according to the BER. Compared to a fixed phase shift in ref.[26], an adjustable phase shift on either the carrier or the information-bearing signal enables better performance by considering the impact of SSBI.

To evaluate the performance of the DD receiver with an optimal transfer function, we also give the BER results of using a −185-ps/nm CD element to realize the transfer function of $h(t)$, as shown in Fig. 7(b). The CSPR is 6 dB, and the phase shift θ of the optimal transfer function is set to 45°. Our proposed scheme shows a 4.4-dB better OSNR sensitivity than that of the scheme using a dispersive element at the 25% FEC threshold. In addition, our proposed scheme reduces the BER by approximately three orders of magnitude at 30-dB OSNR. The performance improvement can be attributed to the elimination of the effect of frequency-selective power fading. Our proposed optimal transfer function $h(t)$ has a weak enhancement on the SSBI because the null point is not within the information-bearing spectrum, which significantly improves the BER performance. We also provide a theoretical BER curve for coherent detection with the CSPR penalty as a benchmark, which considers the carrier-induced power penalty[34].

Numerical characterization of the BER performance with a near-zero guard band

A numerical simulation is conducted to verify the high performance of our proposed scheme with a near-zero guard band. We generate a 300-GBaud dual-SSB 16-QAM Nyquist-shaped signal with a roll-off factor of 0.01. A 1-Hz guard band (−0.5 Hz to 0.5 Hz) is inserted between the LSB and RSB. After loading additive white Gaussian noise, the proposed DD receiver with an optimal transfer function is used to detect the 16-QAM signal. The phase shift θ of the optimal transfer function is set to 45°. We use a CNN to reconstruct the signal and mitigate SSBI. Further details about the simulation setup are provided in Section 1 of Supplementary information.

Figure 8(a) shows the dependence of the simulated BER on CSPR for different schemes under the condition of a 30-dB OSNR. The BER curves for the phase shifts to the signal and carrier nearly overlap, which agrees with the results of the theoretical analysis described in the previous section. The optimal CSPR is 3 dB. Only a near-zero guard band is required for the proposed scheme. The BER penalty relative to the theoretical curve can be attributed to the residual SSBI.

Figure 8(b) depicts the simulated BER performance by varying the OSNR for different schemes under the

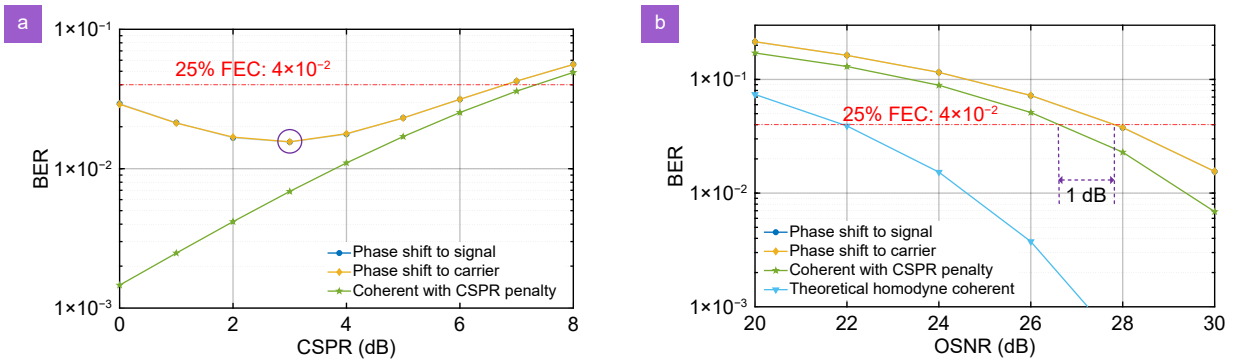

Fig. 8 | (**a**) Simulated BER versus CSPR for different schemes with a 30-dB OSNR. (**b**) Simulated BER versus OSNR for different schemes with a 3-dB CSPR.

condition of a 3-dB CSPR. Compared with a coherent system with a CSPR penalty, the proposed scheme using the optimal transfer function has an approximately 1-dB OSNR penalty, which can be attributed to the residual SSBI. Note that the coherent system compared here considers the CSPR penalty, which is inherent and unavoidable in carrier-assisted DD systems.

Theoretical ESE limit

In this section, we will derive the theoretical ESE limits by invoking Shannon's formula[35]:

$$R = \alpha B \cdot \log_2\left(1 + \frac{\beta_1}{\beta_2}\frac{OSNR}{1+CSPR}\frac{B_{\text{ref}}}{B}\right), \tag{25}$$

where R is the net data rate, α is an interface rate scaling factor, B is the optical signal bandwidth, β_1 is a signal power scaling factor that is related to polarization-division multiplexing, β_2 is a noise enhancement factor, and B_{ref} is 12.5 GHz.

In an amplifier noise-limited system with a DD, if the OSNR and the power of amplified spontaneous emission noise are fixed, then the total power of the signal and carrier is fixed[36]. We assume that the SSBI can be eliminated, which can be achieved by using the receiver structure in Fig. 1(b). In this scenario, the CSPR required by the system is minimal. After PD, the desired carrier-signal beating term and ESNR of the electrical signal can be maximized when the signal power is equal to the carrier power[36,37]. Thus, the lowest optimum CSPR for the proposed scheme is 0 dB.

Because only a near-zero guard band is required at the central frequency of the signal, the electrical bandwidth of the receiver is approximately $B/2$. The *ESE* is expressed as:

$$ESE = \frac{R}{B/2} = \frac{2R}{B}. \tag{26}$$

By substituting Eq. (26) into Eq. (25), we obtain the theoretical ESE limit of the proposed scheme as follows:

$$ESE = 2\alpha \cdot \log_2\left(1 + \frac{\beta_1}{\beta_2}\frac{OSNR}{1+CSPR}\frac{B_{\text{ref}}}{2R}ESE\right), \tag{27}$$

where α, β_1, and β_2 are 1, 2, and 1, respectively. Equation (27) is an implicit function. The bisection method can be used to solve the *ESE*. The theoretical ESE limit mainly depends on the OSNR and net data rate. To comprehensively evaluate the performance of our proposed scheme, we also derive the theoretical ESE limit for coherent homodyne detection.

For coherent detection, the CSPR is $-\infty$ dB. As a coherent receiver mixes a local oscillator with a randomly polarization-rotated signal, it inherently requires a polarization-diverse setup. The *ESE* of the coherent homodyne detection is expressed as

$$ESE = \frac{R/2}{B/2} = \frac{R}{B}. \tag{28}$$

Plugging Eq. (28) into Eq. (25), we obtain the theoretical ESE limit of the coherent homodyne detection as follows:

$$ESE = \alpha \cdot \log_2\left(1 + \frac{\beta_1}{\beta_2}\frac{OSNR}{1+CSPR}\frac{B_{\text{ref}}}{R}ESE\right), \tag{29}$$

where α, β_1, and β_2 are 2, 1, and 1, respectively. After substituting α, β_1, and β_2 into Eq. (27) and Eq. (29), we obtain a unified description of the theoretical ESE limit of the proposed scheme and coherent homodyne as follows:

$$ESE = 2\log_2\left(1 + \frac{OSNR}{1+CSPR}\frac{B_{\text{ref}}}{R}ESE\right). \tag{30}$$

Hence, the difference in the theoretical ESE limit between our proposed scheme and the coherent

homodyne detection is attributed to the CSPR. The optical carrier accounts for a proportion of the total signal power but does not carry any information, which reduces the achievable system performance.

Figure 9(a) shows the theoretical ESE limits for the different schemes. Subsequently, the ESE limit of the proposed scheme is normalized to the coherent-homodyne case, as illustrated in Fig. 9(b). To provide a clearer visual representation, we consider some special cases. Figure 9(c) depicts the normalized theoretical ESE limit of the proposed scheme versus the OSNR for different net rates. As the OSNR increases, the theoretical ESE limit of the proposed scheme gradually approaches that of coherent homodyne detection. The normalized ESE limit is expected to approach 100% if the OSNR is sufficient. Here, the OSNR does not include the carrier power. In addition, as the net rate increases, the normalized ESE limit decreases at a fixed OSNR value. The theoretical derivations of the theoretical ESE limits for the SVR, KK, and CADD receivers are provided in Section 2.1 of Supplementary information. Performance and cost metrics comparing coherent detection and DD schemes at 200-Gb/s net rate and 30-dB OSNR can be found in Section 2.2 of Supplementary information.

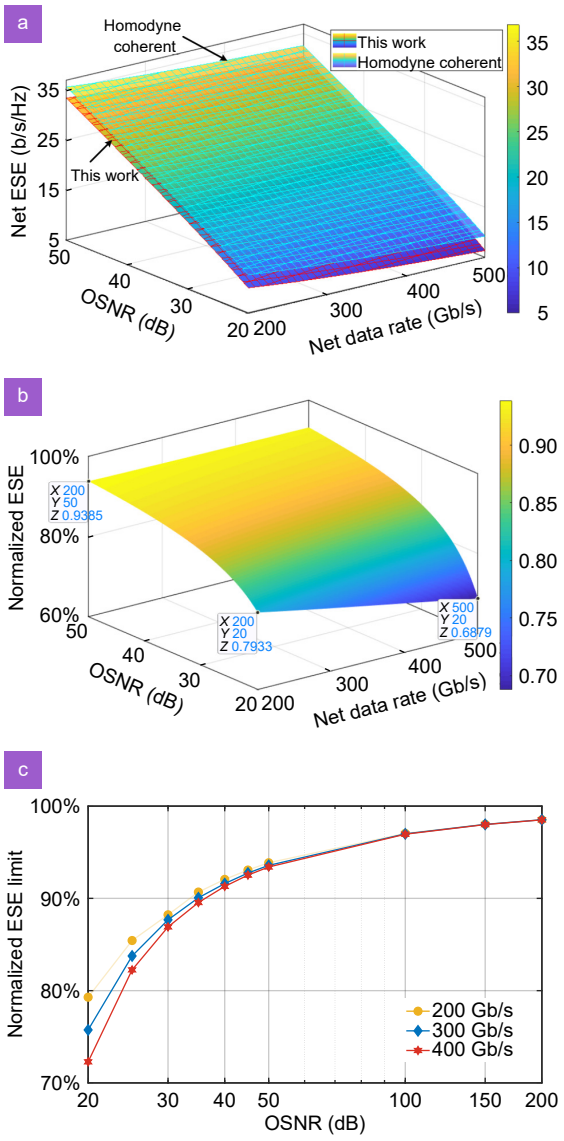

Fig. 9 | (**a**) Theoretical ESE limits for different schemes. (**b**) Normalized theoretical ESE limit of our proposed scheme. (**c**) Normalized theoretical ESE limit of our proposed scheme versus OSNR for different net rates.

Transmission experiment

To verify the feasibility of the proposed DD receiver with an optimal transfer function, we conduct a proof-of-concept experiment with a 46-GBaud 64-QAM signal over an 80-km SMF transmission in which a WS is employed to construct the optimal transfer function. The experimental setup and DSP flow charts are shown in Fig. 10(a) and are described in detail in the Methods section as well as Section 3 of Supplementary information.

Figure 10(b) depicts the optical spectra of the 64-QAM signal measured at different stages using an optical spectrum analyzer (OSA) (APEX AP2040C) with a resolution of 1.12 pm. The bandwidths of both the LSB and RSB signals are 23.23 GHz since the signals are digitally shaped by two root raised cosine (RRC) filters with roll-off factors of 0.01. A 5.77-GHz guard band is inserted between the LSB and RSB due to the limited resolution of the WS. After the WS, the signal suffers from a slight distortion near the carrier, which can be attributed to the fact that the amplitude response of the constructed transfer function is not strictly all-pass. Thus, the transmitted signal will suffer from severe signal distortion and carrier attenuation. The distortion imposed on the spectrum of the information-bearing signal will decrease the BER performance, which is similar to the degradation effect of an imperfect channel. When the carrier is attenuated, a larger CSPR is required, which will sacrifice the effective optical power of the information-bearing signal and reduce the system's performance. It is possible to achieve a flat amplitude response with a single-frequency phase shift by using an all-pass phase filter in silicon-on-insulator[38]. We can observe that an increase in the phase shift leads to greater signal distortion. The inset at the top-right corner of Fig. 10(b) shows an enlarged view of the carrier. We can see that approximately 3-dB and 4-dB optical attenuations are imposed on the carrier when the phase shifts are set to 90° and 110°, respectively. Hence,

the constructed transfer function using the WS is not perfect, as we would prefer it to be.

Figure 10(c) depicts the BER of the 46-GBaud 64-QAM signals by varying the CSPR value at optical back-to-back (OBTB) and after 80-km transmission. In contrast to the scenario of a 90°-phase shift, the scenario of a 110°-phase shift suffers from more severe signal distortion and carrier attenuation, as shown in Fig. 10(b). These two degradations increase the ultimate BER. Despite these challenges, the BER performance of the 110°-phase shift is still better than that of the 90°-phase shift. Consequently, we have experimentally verified that the 110°-phase shift is more suitable for this system than the 90°-phase shift. In practice, we need to judiciously select an appropriate phase shift according to the operating conditions, which can be controlled by monitoring the BER in the receiver through a FEC chip. These results yield solid evidence to support the theoretical analysis. For both the transmission and OBTB cases, the optimum CSPR values are 12 dB, which are the results of a tradeoff between the SSBI and SNR. At CSPR values lower than 12 dB, the signals suffer severe SSBI distortion. A high CSPR contributes to better BER performance because the influence of the SSBI distortion is mitigated.

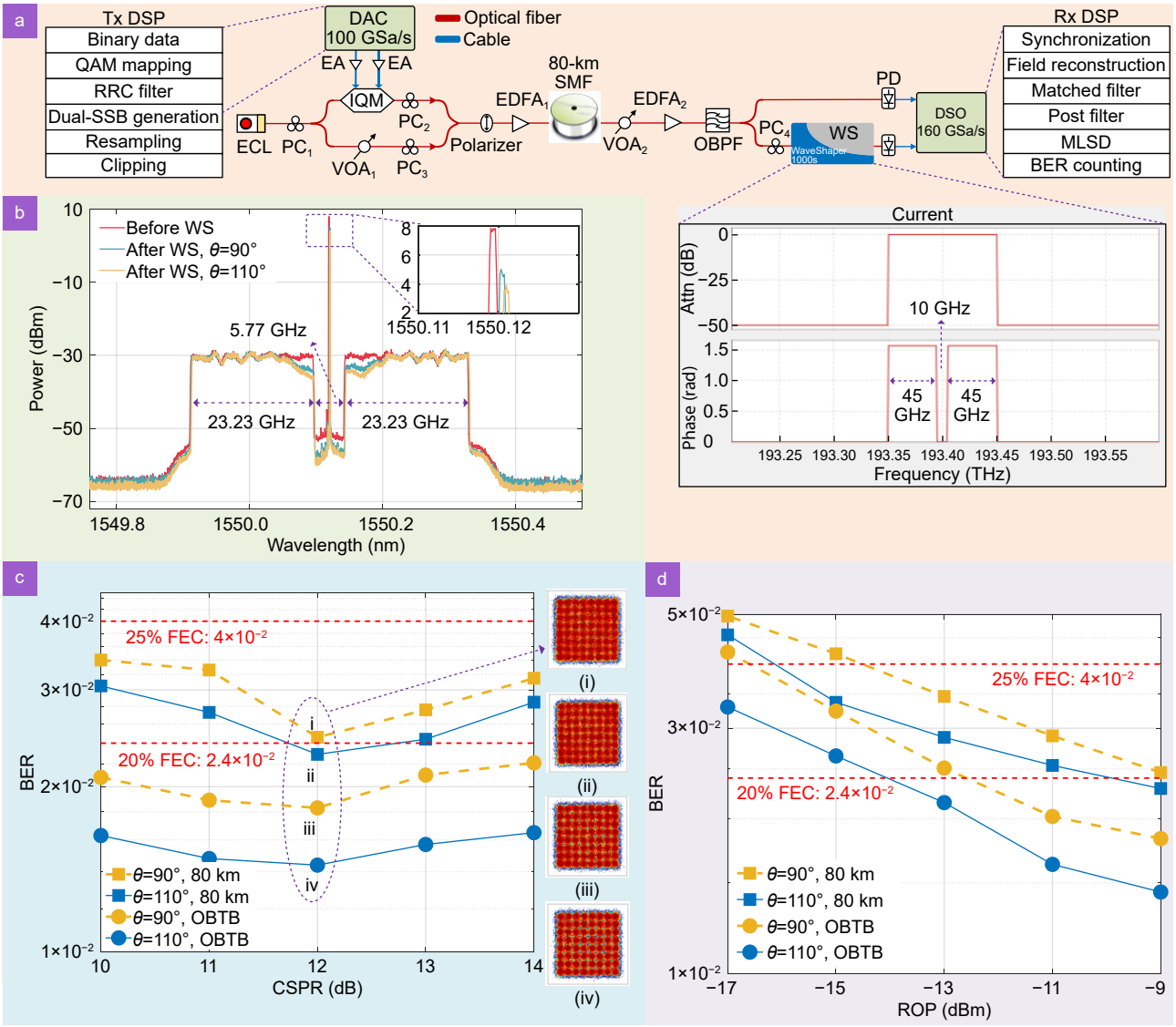

Fig. 10 | (**a**) Experimental setup and DSP flow charts. DAC: digital-to-analog converter; EA: electrical amplifier; IQM: in-phase and quadrature modulator; ECL: external cavity laser; PC: polarization controller; VOA: variable optical attenuator; EDFA: erbium-doped fiber amplifier; OBPF: optical bandpass filter; DSO: digital storage oscilloscope; MLSD: maximum-likelihood sequence decision. (**b**) Optical spectra of the 64-QAM signals measured at different stages. (**c**) BER versus CSPR in the transmission and OBTB cases. Insets (i-iv) show constellations at 12-dB CSPR. (**d**) BER versus ROP in the transmission and OBTB cases.

However, a high CSPR sacrifices the effective optical power of the information-bearing signal, which reduces the achievable system performance. Consequently, increasing the CSPR beyond the optimum value leads to an increase in the BER. In the OBTB case, we use a VOA to replace the 80-km SMF but emulate its insertion loss. The BER gap between the 80-km transmission and the OBTB case is mainly attributed to the quantization noise of the DSO because the peak-to-average-power ratio of the received signals is increased after the 80-km SMF transmission. The recovered constellation diagrams at the optimum CSPR value are shown in the insets.

We also investigate the BER performance versus the received optical power (ROP) in the OBTB and 80-km SMF transmission cases, as shown in Fig. 10(d). We found that a −9-dBm ROP is enough to reach the 20% FEC threshold of 2.4×10^{-2} in both cases. We successfully demonstrate 276-Gb/s 64-QAM signal transmission over an 80-km SMF in a carrier-assisted DD system. Taking into account the 0.5% synchronization sequence and 20% FEC overhead, we obtain a 228.85-Gb/s net rate (46 GBaud × 6 b/symbol × 99.5% / 1.2) and an 8.76-b/s/Hz net ESE (228.85 Gb/s / 26.12 GHz). The proposed scheme enables a record net ESE per polarization per wavelength on DD transmission beyond a 40-km SMF.

Discussion

Table 1 compares the state-of-the-art transmission results of various DD schemes. We successfully demonstrate a net 228.85 Gb/s 64-QAM signal transmission over an 80-km SMF with a net ESE of 8.76 b/s/Hz without probabilistic constellation shaping. Compared with our previous work using a dispersion diversity receiver in ref.[25], we achieve a 15% and 23.9% improvement in the net rate and ESE, respectively. Moreover, the structure of the dispersion diversity receiver is simplified by using the proposed receiver, since only one WS, two PDs, and two ADCs are required. In ref.[20], the JSDD receiver achieves an ESE of 9.2 b/s/Hz, but its transmission distance is 40 km. As stated in ref.[39], doubling the transmission reach at a fixed spectral efficiency is a similar achievement as improving the spectral efficiency by 1 b/s/Hz at a fixed reach. A comprehensive metric, denoted $2^{\mathrm{ESE}}\times$Reach, has been proposed to compare optical fiber communication systems[40]. In terms of this metric, we achieve the highest $2^{\mathrm{ESE}}\times$Reach per polarization per wavelength for DD transmission. Besides, a WaveShaper (II-IV 4000A) was also employed in the experimental setup of JSDD. In principle, JSDD is similar to CADD because the quadrature component is detected by using delay lines in both schemes. Their theoretical ESE limits are considerably lower than that of our scheme, as discussed in Section 2.2 of Supplementary information. Figure 11 shows a visual representation of the state-of-the-art transmission results for the DD systems. The proposed scheme achieves a record net ESE of 8.76 b/s/Hz for single-polarization and single-wavelength DD transmission beyond 40-km SMF.

Because of the limited resolution of the WS, a large guard band of 5.77 GHz is required in our experiment, which limits the achievable ESE of the proposed scheme. According to theoretical analysis, only a near-zero guard band is required at the central frequency of the signal. Thus, finding a better physical implementation of $h(t)$ is also an important direction for our future efforts. This may be possible by leveraging the burgeoning SiP technology[42–45], such as high-resolution phase filter[46] and high quality factor silicon nitride resonator[47]. A CMOS

Table 1 | Comparisons of the state-of-the-art transmission results per polarization per wavelength on DD systems.

Receiver schemes	Baud rate (GBaud)	Modulation format	Net rate (Gb/s)	Receiver bandwidth (GHz)	ESE (b/s/Hz)	Reach (km)	$2^{\mathrm{ESE}}\times$ Reach	Constellation shaping
GS[13]	40	16-QAM	140	40	3.5	40	452.55	No
KK[10]	85	64-QAM	432	90	4.8	80	2228.61	No
IM-DD[7]	200	PAM-16	494.5	100	4.9	0.12	3.58	Yes
CADD[17]	70	16-QAM	226	36.5	6.2	80	5881.34	No
ASCD[26]	52	32-QAM	208	29.3	7.1	40	5487.48	No
SVR[11]	48	64-QAM	223	32.82	6.79	260	28771.8	Yes
DLEDD[25]	50	32-QAM	199	28.13	7.07	80	10749.1	No
Dual-SSB 32-QAM[41]	60	32-QAM	254.3	33.16	7.67	80	16292.59	No
JSDD[20]	106	64-QAM	520	56.5	9.2	40	23525.34	Yes
This work	46	64-QAM	228.85	26.12	**8.76**	80	**34682.69**	No

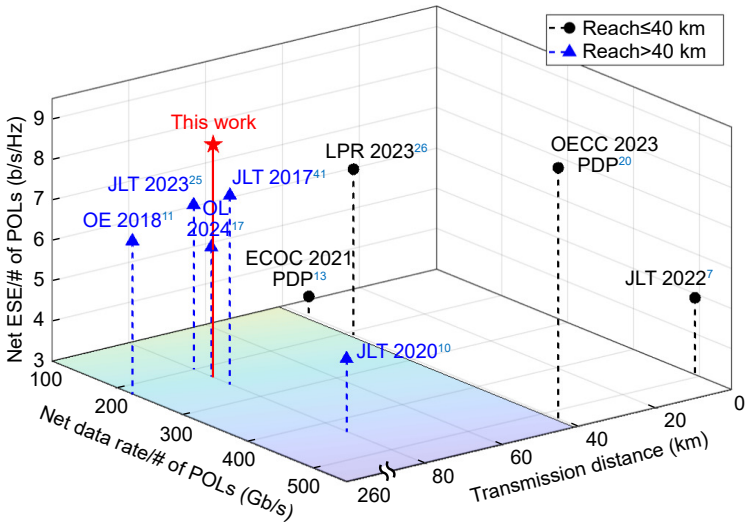

Fig. 11 | Visual representation of the state-of-the-art transmission results on DD systems. POLs: polarizations.

temperature control circuit can be used to realize wavelength alignment between the signal and the filter[48]. Compared with coherent detection, our proposed scheme does not require a LO laser with bulky cooling components, which makes it well-positioned for full integration. In DSP, our proposed scheme does not need a signal equalization and carrier recovery algorithm. Note that our proposed scheme is based on a single-polarization configuration, to further improve the transmission capacity and ESE, polarization multiplexing transmission with two single-polarization receivers can be used, where a controllable polarization rotator and a polarization beam splitter are needed to split the polarization-division multiplexed signal[16].

Conclusions

To approach the ESE of coherent homodyne detection using DD, we have derived an optimal DD receiver architecture with the simplest design, which comprises a coupler, two single-ended PDs, two ADCs, and a frequency-selective phase shifter with an optimal transfer function. By considering the impact of both noise and SSBI on system performance, the optimal transfer function exhibits an all-pass amplitude response accompanied by a phase response that introduces an adjustable phase shift on either the carrier or the information-bearing signal. In practice, we need to judiciously select an appropriate phase shift according to the operating conditions. Because the null point is not within the information-bearing spectrum, the SSBI enhancement is weak. Only a near-zero guard band is required at the signal's central frequency, which contributes to the ESE of the proposed scheme approaching that of a coherent homodyne. By invoking Shannon's formula, we have derived the theoretical ESE limit for various detection schemes, which is dependent on the net rate and OSNR. The proposed scheme is closest to the coherent homodyne in the theoretical ESE limit. The simulation results indicate that our proposed scheme has only an approximately 1-dB OSNR penalty at the 25% FEC threshold, compared with the coherent transmission system. Compared to the scheme using a dispersive element, the proposed scheme exhibits a 4.4-dB better OSNR sensitivity at the 25% FEC threshold and reduces the BER by approximately three orders of magnitude at an OSNR of 30 dB.

Furthermore, we have performed a proof-of-concept experiment by leveraging the WS to construct an optimal transfer function. Using a 110°-phase shift, we have achieved a 228.85-Gb/s net rate and 8.76-b/s/Hz net ESE by transmitting a 46-GBaud 64-QAM signal in an 80-km SMF without probabilistic constellation shaping. To the best of the knowledge, we report a record net ESE for single-polarization and single-wavelength DD transmission beyond a 40-km SMF. For a comprehensive metric denoted as $2^{\mathrm{ESE}}\times$Reach, we achieve the highest $2^{\mathrm{ESE}}\times$Reach for single-polarization and single-wavelength DD transmission. We believe that the proposed DD receiver with an optimal transfer function may pave the way for new applications in large-capacity and cost-effective data center interconnections, metro networks, and mobile backhauls.

Methods

Experimental setup

Figure 10(a) illustrates the experimental setup. We generate a 46-GBaud dual-SSB 64-QAM signal with an approximately 6-GHz guard band (–3 GHz to 3 GHz) by using a 100-GSa/s DAC (MICRAM DAC10002) with a 3-dB bandwidth of 35 GHz. The electrical QAM signal is amplified by two EAs (SHF S807 C) and then used to drive an IQM (Fujitsu FTM7992HM) with a 3-dB bandwidth of 35-GHz. The IQM is biased at its transmission null. An ECL with an approximately 15-kHz linewidth outputs a 1550-nm continuous-wave light. The narrow linewidth source is employed due to the length mismatch between the carrier branch and the information-bearing signal branch[49]. Such a length mismatch can be avoided in the photonic integrated circuit with an appropriate design. The continuous-wave light is split into two branches. One part is coupled to the IQM to produce an optical dual-SSB 64-QAM signal, and the other serves as a carrier. The 64-QAM signal and carrier are then combined to construct a CV-DSB signal using a coupler. The CV-DSB signal in this work is a traditional coherent QAM signal with a guard band. The polarization states of the QAM signal and carrier are aligned along the axis of the polarizer by using two PCs and a polarizer[15]. We adjust the CSPR of the CV-DSB signal by employing a VOA. After amplifying to 7 dBm with an EDFA, the CV-DSB signal is launched into an 80-km SMF spool for transmission.

On the receiver side, the second VOA is used to vary the ROP of the CV-DSB signal and emulate the OBTB case. We use an EDFA to amplify the CV-DSB signal and an OBPF to reject out-of-band noise. The DD receiver with an optimal transfer function is composed of a PC, two PDs, and a WS (Finisar WaveShaper 1000s). The PC is used to align the polarization of the incident signal to the polarization of the WS. The inset in Fig. 10(a) presents the setup of the WS. Because the bandwidth of the CV-DSB signal is approximately 52 GHz, we construct a 100-GHz optimal transfer function with an all-pass amplitude response centered at 1550 nm. Here, due to the limited resolution of the WS, we cannot achieve a single-frequency phase shift in the experiment. We use a 10-GHz guard band, which is slightly larger than the guard band of the CV-DSB signal. Our goal is to achieve a fully integrated DD receiver based on low-cost frequency-selective phase shifter, which can be realized by using a high-resolution phase filter[46] or high quality factor silicon nitride resonator[47]. Finally, the electrical signals are captured by a two-channel 59-GHz DSO (LeCroy 10-59Zi-A) operating at 160 GSa/s.

DSP algorithm

Figure 10(a) shows the DSP configuration. In the transmitter DSP stack, the binary data is first mapped onto 204800 64-QAM symbols for two independent LSB and RSB. The random binary strings are constructed using the Mersenne Twister algorithm. Then, two RRC filters are used to produce the corresponding Nyquist-shaped LSB and RSB signals at the roll-off factors of 0.01. Next, we combine the LSB and RSB signals to generate a dual-SSB 64-QAM signal with a guard band. After resampling and clipping, the signal is uploaded to the two channels of the DAC.

In the receiver DSP stack, the captured two-channel signals are first synchronized. To realize the field reconstruction of the CV-DSB signal, the two-channel signals are processed by a deep CNN with the same network structure as that described in ref.[25]. In the deep CNN, 60% of the data samples are used for training and the remaining 40% samples for testing because of the limited memory of the DAC. The kernel sizes are set to 19 and 1 for the convolutional layers and shortcut connections, respectively. After field reconstruction, the CV-DSB signal is decomposed via down-conversion and a matched filter. We use a 2-tap post filter and an MLSD to suppress the enhanced noise[50]. One BER value is averaged from four measurements. Thus, the BER is obtained by counting approximately 2×10^6 bits, which are sufficient for testing BERs of approximately 10^{-2}.

References

1. Xie YW, Hong SH, Yan H et al. Low-loss chip-scale programmable silicon photonic processor. *Opto-Electron Adv* **6**, 220030 (2023).
2. Xu ZY, Niu WQ, Liu Y et al. 31.38 Gb/s GaN-based LED array visible light communication system enhanced with V-pit and sidewall quantum well structure. *Opto-Electron Sci* **2**, 230005 (2023).
3. Xie CJ, Zhang B. Scaling optical interconnects for hyperscale data center networks. *Proc IEEE* **110**, 1699–1713 (2022).
4. Wan YJ, Liu XD, Wu GZ et al. Efficient stochastic parallel gradient descent training for on-chip optical processor. *Opto-Electron Adv* **7**, 230182 (2024).
5. Khonina SN, Kazanskiy NL, Butt MA et al. Optical multiplexing techniques and their marriage for on-chip and optical fiber communication: a review. *Opto-Electron Adv* **5**, 210127 (2022).
6. Fan QR, Zhou G, Gui T et al. Advancing theoretical understanding

and practical performance of signal processing for nonlinear optical communications through machine learning. *Nat Commun* **11**, 3694 (2020).
7. Che D, Chen X. Higher-order modulation vs faster-than-Nyquist PAM-4 for datacenter IM-DD optics: an AIR comparison under practical bandwidth limits. *J Lightwave Technol* **40**, 3347–3357 (2022).
8. Zhong KP, Zhou X, Huo JH et al. Digital signal processing for short-reach optical communications: a review of current technologies and future trends. *J Lightwave Technol* **36**, 377–400 (2018).
9. Mecozzi A, Antonelli C, Shtaif M. Kramers–Kronig coherent receiver. *Optica* **3**, 1220–1227 (2016).
10. Le ST, Schuh K, Dischler R et al. Beyond 400 Gb/s direct detection over 80 km for data center interconnect applications. *J Lightwave Technol* **38**, 538–545 (2020).
11. Che D, Sun C, Shieh W. Maximizing the spectral efficiency of stokes vector receiver with optical field recovery. *Opt Express* **26**, 28976–28981 (2018).
12. Che D, Chandrasekhar S, Chen X et al. Single-channel direct detection reception beyond 1 Tb/s. In *Optical Fiber Communications Conference and Exhibition*1−3 (IEEE, 2019); http://doi.org/10.1364/OFC.2019.Th4B.7.
13. Chen HS, Fontaine NK, Mazur M et al. 140G/70G direct detection PON with >37 dB power budget and 40-km reach enabled by colorless phase retrieval full field recovery. In *European Conference on Optical Communication* 1−4 (IEEE, 2021); http://doi.org/10.1109/ECOC52684.2021.9605860.
14. Shieh W, Sun C, Ji HL. Carrier-assisted differential detection. *Light Sci Appl* **9**, 18 (2020).
15. Li JC, Wang Z, Ji HL et al. High electrical spectral efficiency silicon photonic receiver with carrier-assisted differential detection. In *Optical Fiber Communication Conference and Exhibition* (OFC, 2022); http://doi.org/10.1364/OFC.2022.Th4B.6.
16. Li J, Wang Z, Li X et al. Net 426-Gb/s and 11.83-b/s/Hz 80-km transmission with an integrated SiP dual-polarization direct detection receiver. In *European Conference on Optical Communications* 1710−1713 (IEEE, 2023); http://doi.org/10.1049/icp.2023.2673.
17. Li JC, Wang Z, Li XF et al. Modified SiP single-polarization CADD receiver. *Opt Lett* **49**, 1133–1136 (2024).
18. Li XY, O'Sullivan M, Xing ZP et al. Asymmetric self-coherent detection. *Opt Express* **29**, 25412–25427 (2021).
19. Hu YX, Li XY, Mao D et al. Transmission of net 200 Gbps/λ over 40 km of SMF using an integrated SiP phase-diverse receiver. In *European Conference on Optical Communications* 1−4 (IEEE, 2022). https://ieeexplore.ieee.org/document/9979400
20. Wu Q, Li XY, Zhu YX et al. Single-wavelength net 1 Tb/s transmission in SMF and 6.4 Tb/s in weakly-coupled 7-core MCF using a phase- and polarization-diverse direct detection receiver in jones space. In *Opto-Electronics and Communications Conference* 1−4 (IEEE, 2023); http://doi.org/10.1109/OECC56963.2023.10209682.
21. Wu Q, Zhu YX, Li XY et al. Four-dimensional direct detection receiver enabling Jones-space field recovery with phase and polarization diversity. *Photonics Res* **12**, 399–410 (2024).
22. Li XF, An SH, Ji HL et al. Deep-learning-enabled high-performance full-field direct detection with dispersion diversity. *Opt Express* **30**, 11767–11788 (2022).
23. Li XF, An SH, Li JC et al. Deep-learning enabled direct detection of 42-GBaud complex-valued DSB 16-QAM signal. In *Conference on Lasers and Electro-Optics* (Optica Publishing Group, 2022); http://doi.org/10.1364/CLEO_SI.2022.SW4E.4.
24. Li XF, Li JC, An SH et al. Deep-learning-enabled high electrical-spectral-efficiency direct detection with reduced computation complexity. In *Optical Fiber Communication Conference* (Optica Publishing Group, 2023); http://doi.org/10.1364/OFC.2023.M2F.2.
25. Li XF, Li JC, An SH et al. Deep-learning-enabled direct detection with reduced computational complexity and high electrical-spectral-efficiency. *J Lightwave Technol* **41**, 5495–5502 (2023).
26. Zhang JS, Li XY, Hu YX et al. Spectrally efficient integrated silicon photonic phase-diverse DD receiver with near-ideal phase response for C-band DWDM transmission. *Laser Photonics Rev* **18**, 2300623 (2024).
27. Liu GN, Zhang L, Zuo TJ et al. IM/DD transmission techniques for emerging 5G fronthaul, DCI, and metro applications. *J Lightwave Technol* **36**, 560–567 (2018).
28. Liu X. Enabling optical network technologies for 5G and beyond. *J Lightwave Technol* **40**, 358–367 (2022).
29. Karar AS, Falou ARE, Barakat JMH et al. Recent advances in coherent optical communications for short-reach: phase retrieval methods. *Photonics* **10**, 308 (2023).
30. Bo TW, Kim H. DC component recovery in kramers-kronig receiver utilizing AC-coupled photo-detector. *J Lightwave Technol* **38**, 4307–4314 (2020).
31. Hao JY, Lin X, Lin YK et al. Lensless complex amplitude demodulation based on deep learning in holographic data storage. *Opto-Electron Adv* **6**, 220157 (2023).
32. Que ZQ, Zhu YX, Fan HX et al. Mapping large LSTMs to FPGAs with weight reuse. *J Signal Process Syst* **92**, 965–979 (2020).
33. Molchanov P, Tyree S, Karras T, et al. Pruning convolutional neural networks for resource efficient inference. arXiv: 1611.06440 (2016); http://doi.org/10.48550/arXiv.1611.06440.
34. Proakis J G. *Digital Communications* 4th ed (McGraw-Hill, Boston, 2001).
35. Chen X, Chandrasekhar S, Winzer P J. Self-coherent systems for short reach transmission. In *European Conference on Optical Communication* 1–3 (IEEE, 2018); http://doi.org/10.1109/ECOC.2018.8535234.
36. Li A, Peng WR, Cui Y et al. Single-λ 112Gbit/s 80-km transmission of PAM4 signal with optical signal-to-signal beat noise cancellation. In *Optical Fiber Communications Conference and Exposition* 1–3 (Optica Publishing Group, 2018); http://doi.org/10.1364/OFC.2018.Tu2C.5.
37. Che D, Chen X, He JY et al. 102.4-Gb/s single-polarization direct-detection reception using signal carrier interleaved optical OFDM. In *Optical Fiber Communication Conference* (Optica Publishing Group, 2014); http://doi.org/10.1364/OFC.2014.Tu3G.7.
38. Jiang WJ, Xu L, Liu YF et al. Optical all-pass filter in silicon-on-insulator. *ACS Photonics* **7**, 2539–2546 (2020).
39. Klaus W, Winzer PJ, Nakajima K. The role of parallelism in the evolution of optical fiber communication systems. *Proc IEEE* **110**, 1619–1654 (2022).
40. Winzer PJ. Energy-efficient optical transport capacity scaling through spatial multiplexing. *IEEE Photonics Technol Lett* **23**, 851–853 (2011).
41. Zhu YX, Ruan XK, Zou KH et al. Beyond 200G direct detection

transmission with Nyquist asymmetric twin-SSB signal at C-band. *J Lightwave Technol* **35**, 3629–3636 (2017).
42. Shekhar S, Bogaerts W, Chrostowski L et al. Roadmapping the next generation of silicon photonics. *Nat Commun* **15**, 751 (2024).
43. Pandey A, Mi ZT. Multi-wavelength nanowire micro-LEDs for future high speed optical communication. *Opto-Electron Adv* **7**, 240011 (2024).
44. Su YK, Zhang Y, Qiu CY et al. Silicon photonic platform for passive waveguide devices: materials, fabrication, and applications. *Adv Mater Technol* **5**, 1901153 (2020).
45. Zhang RH, Li XF, He Y et al. Ultra-high bandwidth density and power efficiency chip-to-chip multimode transmission through a rectangular core few-mode fiber. *Laser Photonics Rev* **17**, 2200750 (2023).
46. Kaushal S, Aadhi A, Roberge A et al. All-fibre phase filters with 1-GHz resolution for high-speed passive optical logic processing. *Nat Commun* **14**, 1808 (2023).
47. Ji XC, Roberts S, Corato-Zanarella M et al. Methods to achieve ultra-high quality factor silicon nitride resonators. *APL Photonics* **6**, 071101 (2021).
48. Zhang H, Huang BJ, Zhang Z et al. Monolithic integration of CMOS temperature control circuit and Si_3N_4 microring filters for wavelength stabilization within ultra wide operating temperature range. *IEEE J Sel Top Quantum Electron* **26**, 8200407 (2020).
49. Zhou X, Gao YY, Huo JH et al. Theoretical analysis of phase noise induced by laser Linewidth and mismatch length in self-homodyne coherent systems. *J Lightwave Technol* **39**, 1312–1321 (2021).
50. Zhong KP, Zhou X, Gao YL et al. 140-Gb/s 20-km transmission of PAM-4 signal at 1.3 μm for short reach communications. *IEEE Photonics Technol Lett* **27**, 1757–1760 (2015).

Acknowledgements

This work was supported by the National Natural Science Foundation of China (62341508).

Competing interests

The authors declare no competing financial interests.

Supplementary information

Supplementary information for this paper is available at https://doi.org/10.29026/oes.2025.240020

Scan for Article PDF